SHORT COMMUNICATION

Reduction kinetics of nickel-based supporting anode composite substrates under operating conditions of intermediate-temperature solid oxide fuel cells

A. U. Sharafutdinov[1] · D. A. Agarkov[1] · I. N. Burmistrov[1] · D. S. Katrich[1] · G. M. Korableva[1] · A. V. Samoilov[1] · I. I. Tartakovskii[1] · S. I. Bredikhin[1]

Abstract

Nickel oxide reduction kinetics and formation of the electric potential of anode-supported solid oxide fuel cell (SOFC) were studied using in situ Raman spectroscopy (RS) and conventional electrochemical techniques. It was shown that the time dependence of the electric potential and the intensity of the Raman spectra during anode substrate reduction can be conditionally divided into two stages. At the initial stage, in the first seconds after hydrogen supply, the open circuit voltage (OCV) quickly rises and stabilizes at a value of about 0.85 V. This stage is not accompanied by noticeable changes in RS. Then, there is a more gradual rise, requiring tens of minutes, to the OCV equilibrium value. The beginning of the second stage of the increase in the OCV coincides with a sharp change in the intensity of the specific spectral line in the Raman spectrum. An increase of the OCV in the first seconds after hydrogen supply is explained by an increase in the hydrogen concentration at the outer boundary of the SOFC anode. The sharp change in the intensity of the Raman spectrum, in turn, can be explained by the reduction of NiO to the metallic state in the near electrolyte region. In this work, a detailed reduction model of the NiO-YSZ (yttria-stabilized zirconia) cermet composite supporting substrate of an anode-supported SOFC was constructed. The model was developed on the assumption that the rate of the nickel oxide reduction reaction at each point of the sample depends only on the partial pressure of hydrogen, the fraction of oxidized nickel, and temperature. In the case of repeated reduction and at high temperatures, it can be assumed that the reaction has first-order kinetics, i.e., reaction rate is proportional to the fraction of oxidized nickel. At primary reduction and temperatures of 400–600 °C, the reaction is described by Avrami-Erofeev kinetics.

Keywords Solid oxide fuel cell · SOFC · Anode-supported SOFC · Anode substrate · Reduction kinetics · Raman scattering · Chronopotentiometry · Reduction model · Cermet

Introduction

Solid oxide fuel cells (SOFCs) are electrochemical devices that directly convert the chemical energy of the oxidation of hydrogen and gaseous hydrocarbons into electrical and high-potential thermal energy. Power plants based on SOFC stacks have a record efficiency among electric power generators: the efficiency exceeds 60% [1], and taking into account high-potential thermal energy, it exceeds 90% [2, 3].

SOFC is a multilayer ceramic assembly consisting of a gas-tight electrolyte, porous anode, and cathode. Air is supplied to the cathode of the cell, where molecular oxygen is reduced to O^{2-} anions. Due to the difference in the chemical potential of oxygen through the electrolytic membrane, oxygen anions, newly formed at the cathode of the cell, migrate to the anode, where, in turn, the fuel is oxidized (H_2 or synthesis gas obtained from hydrocarbons) with the formation of water (and carbon dioxide in case of synthesis gas supply) and free electrons. When connected to a load element, an electric current flows through a closed circuit [4].

The technology of SOFC with an electrolyte-supported structure, so called the first generation SOFC, has received the widest development. For the most part, this is due to the peculiarities of manufacturing a single SOFC. In the

✉ D. A. Agarkov
agarkov@issp.ac.ru

1 Osipyan Institute of Solid State Physics RAS, 2 ul. Acad. Osipyana, 142432 Chernogolovka, Russia

electrolyte-supported structure, the main mechanical load is carried by the solid electrolyte membrane, which is an anionic conductor located in the center of the cell. The membrane formation temperature lies above 1450 °C. In turn, standard electrode materials, which are made directly on both surfaces of the ceramic membrane (with the thickness of 150–200 μm), are formed at significantly lower temperatures (1100–1300 °C), which makes it possible to manufacture plane-parallel defect-free SOFCs [5–7].
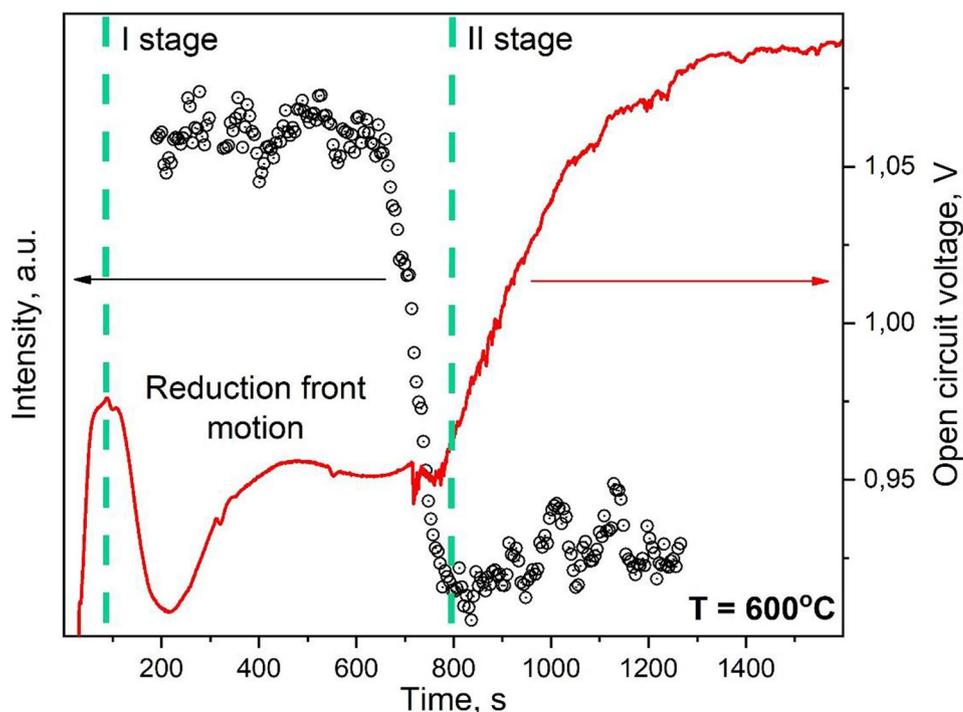
Second-generation SOFCs include cells with anode-supported structure. The main difference from SOFC of the first generation is the transition from anionic membranes with a thickness of 150–200 μm to thin-film membranes with a thickness of 5–10 μm [8–11]. Currently, among commercial power plants based on SOFC technology, electrochemical generators based on SOFC with a supporting anode substrate are most widely used. The basis of such an SOFC is a substrate based on nickel oxide and an anion-conducting material. Since the sintering of all layers of the membrane-electrode assembly takes place in an air atmosphere, before starting electrochemical tests, it is necessary to reduce nickel oxide, which is part of the anode electrode, to a metallic state. Incomplete reduction or significant non-uniform reduction of the anode substrate can affect both the mechanical stability of the SOFC and its electrochemical performance. For this reason, the study of the kinetics of the supporting anode substrate reduction is an extremely urgent and significant task.

In our previous works [12–14], the kinetics of the formation of the electric potential of SOFCs with a supporting anode substrate was studied using in situ Raman spectroscopy (RS) and conventional electrochemical techniques. The studies were carried out using a combined technique developed and created at the Osipyan Institute of Solid State Physics RAS (Russia). This technique combines the opportunities of in situ RS, as well as electrochemical techniques and gas analysis [15–17].

In the previous work [12], fuel cell open-circuit voltage (OCV) during the reduction of fuel cell anode in the hydrogen atmosphere was measured. In the same time, the intensity of 1100 cm^{-1} line in the Raman spectrum of the electrolyte-anode boundary was monitored. It was shown that the time dependence of the potential and intensity of the Raman spectra can be conditionally divided into two stages (Fig. 1).

At the initial stage, in the first seconds after hydrogen supply, the OCV quickly rises and stabilizes at a value of about 0.85 V. This stage is not accompanied by any noticeable changes in the Raman spectra. Then, there is a more gradual rise, requiring tens of minutes, to the OCV equilibrium value. The beginning of the second stage of the increase of the OCV coincides with a sharp change in the intensity of 1100 cm^{-1} line in the Raman spectrum. An increase of the OCV during first seconds after hydrogen supply is explained by an increase in the hydrogen concentration at the outer boundary of the SOFC anode. The sharp change in 1100 cm^{-1} line intensity of the Raman spectrum,

Fig. 1 Time dependence of the intensity of 1100 cm^{-1} line in the Raman spectra (points) and OCV on a SOFC model sample (line) for a reduction operating temperature of 600 °C [12, 18]. The left dotted line corresponds to the start of the first stage of the reduction reaction, the right one corresponds to the start of the second one. Between them, the shifting of a reduction front in the sample is assumed

in turn, can be explained by the reduction of nickel oxide to the metallic state in the near-electrolytic region.

In the present work, a more detailed model for the reduction of a cermet composite NiO-YSZ (92 mol.% ZrO_2 + 8 mol.% Y_2O_3) supporting substrate of an anode-supported SOFC was developed. The model was built on the assumption that the rate of the nickel oxide reduction reaction at each point of the sample depends only on the partial pressure of hydrogen, the fraction of oxidized nickel, and temperature. In the case of repeated reduction at high temperatures, it can be assumed that the reaction has first-order kinetics, i.e., it depends only on the fraction of nickel oxidized to the first degree. At primary reduction and temperatures of 400–600 °C, the reaction is described by Avrami-Erofeev kinetics.

Experimental section

For current research, a model sample of a solid oxide fuel cell with a supporting anode substrate was fabricated. A two-layer anode substrate (600 μm thick current-collecting and 40 μm thick functional sublayers) with a 9 μm thick thin-film electrolyte with the composition of 8YSZ (92 mol.% ZrO_2 + 8 mol.% Y_2O_3) was used as a carrier substrate [19]. An anode substrate with a thin-film electrolyte with the size of 100 × 100 mm was cut into disks with the diameter of 21 mm using a compact precision marker MiniMarker 2-20A4 based on a fiber laser.

The cathodic functional layer based on LSCF-6428-N paste [20] with the composition of $(La_{0.6}Sr_{0.4})_{0.97}Co_{0.2}Fe_{0.8}O_{3-d}$ and a specific surface area of 10–15 m^2/g was applied to the anode substrate with a thin-film electrolyte by screen printing technique using an Ekra E2 machine using mesh #32 (32 threads per 1 cm). The cathode electrode was deposited using a mesh with a hole that made it possible to transmit light radiation and detect Raman scattered radiation from the internal interface of a model SOFC. Such sample geometry is described in our previous manuscripts [21–23] and patents [15–17]. After deposition, the cathode electrode was dried at a temperature of 80 °C and high temperature annealed according to the temperature profile shown in Fig. 2.

A complex heating profile is necessary for optimal removal of organic components, the maximum formation temperature was 1000 °C, and the annealing time at this temperature was equal to 1.5 h. The thickness of the cathode layer after sintering was equal to 11 μm.

After application of the cathode electrode, gold electrodes were applied to both sides of the model sample, which were fired at a temperature of 900 °C for 1 h. Gold wires with the diameter of 0.2 mm were connected to gold electrodes for electrochemical studies.

For the optical studies, a pin-hole was prepared in the cathode of the sample (Fig. 3). In combination with an optically transparent electrolyte, this hole makes it possible to

Fig. 2 Heating profile of high-temperature annealing of the cathode electrode of a model SOFC
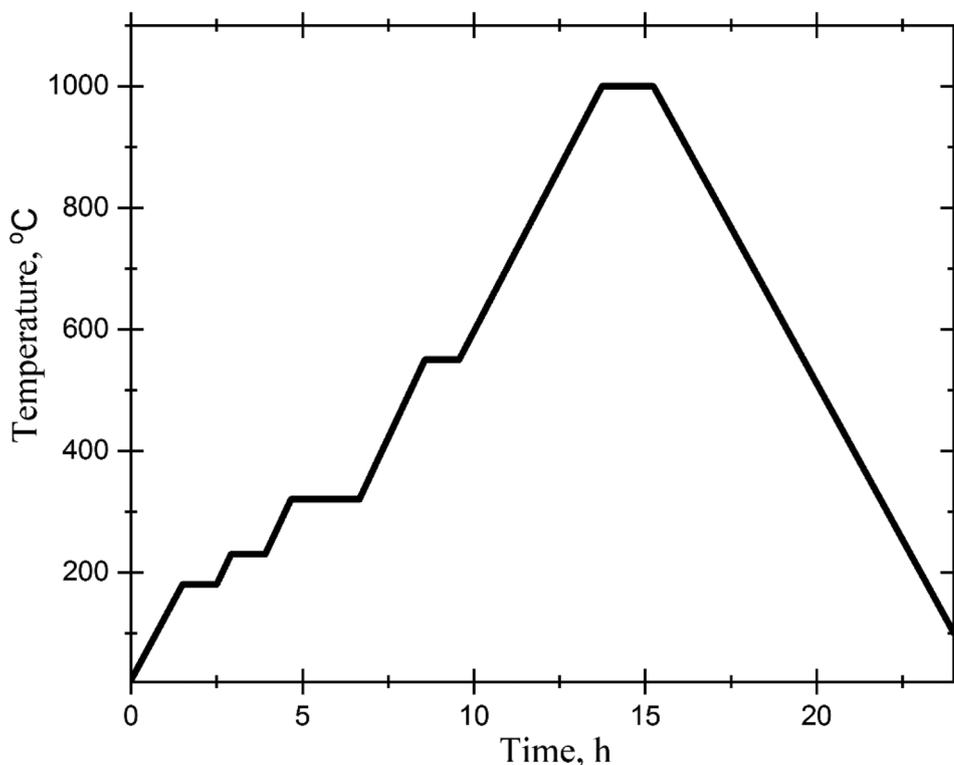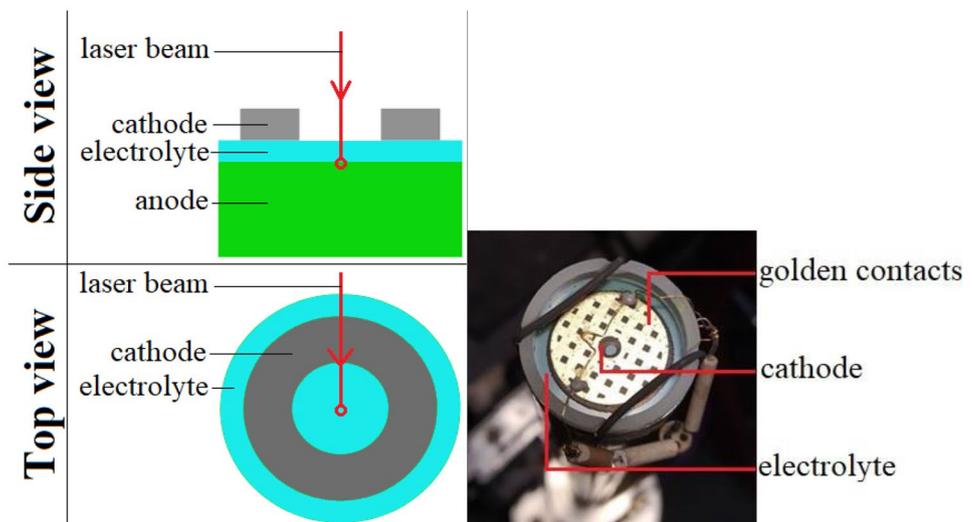
Fig. 3 Scheme of a model sample with an indication of the laser beam direction (left); a photograph of the model sample in the measuring cell (right)

study directly the anode|electrolyte inner interface. The measuring cell, equipped with a gas mixtures supply system, was placed in a high-temperature furnace in order to ensure the operating conditions of SOFC.

Electrochemical and optical studies of the model sample were carried out using a combined technique that gives opportunity to carry out the simultaneous measurements using conventional electrochemical methods (study of current–voltage and power characteristics, chronopotentiometry, impedance studies), as well as using Raman spectroscopy. The technique is described in detail in previous works [14, 21–24].

In the optical part of the facility, a multimode green laser with a power of 20 mW passes through an optical system in order to create a monochromatic beam with a wavelength of 532 nm, which is directed by a movable mirror onto the sample. Scattered radiation is collected by a system of lenses into a beam, which passes through an edge filter to cut off the exciting radiation, and enters a monochromator (MDR-12, LOMO, Russia). The radiation decomposed into a spectrum is fed into a liquid nitrogen-cooled Roper Scientific LN/CCD-1340/400-EHRB/1 CCD camera (1340×400 pixels, Netherlands), the data from which is sent to a computer and processed by the WinSpec software.

As for the chronopotentiometric studies, a Gamry Reference 3000 potentiostat–galvanostat was used in this work.

Results and discussion

Experimental model development

Reduction kinetics

The basis for model development was the assumption that the rate of the nickel reduction reaction $Q(T, p_{H_2}, x_{NiO})$ at each point of the sample depends on the temperature T, the partial pressure of hydrogen p_{H_2}, and the fraction of oxidized nickel x_{NiO}.

Based on the literature data [25], the reduction kinetics of thin nickel oxide layers (25 μm) is quite fast and has an activation character, which is reflected in the following expression for the topochemical rate of the reduction reaction k_c:

$$k_c = 2.6 * 10^5 \exp(-E_a/kT) \left[\frac{cm}{s} \right], \tag{1}$$

where $E_a = 1.0 eV$ is activation energy.

At the moment, the effect of partial pressures of hydrogen and water on the reaction rate is poorly understood, so we used the results of work [26], where at a temperature of 500 °C, up to a certain threshold, a linear dependence of the reduction rate on the partial pressures of water p_{H_2O} and hydrogen p_{H_2} was detected:

$$Q(T, p_{H_2}, x_{NiO}) = k_c S_V/RT(p_{H_2} - \gamma p_{H_2O}) f(x_{NiO}), \tag{2}$$

where S_V is the specific surface area of nickel particles, $\gamma = \frac{p_{H_2}^{th}}{p_{H_2O}^{th}}$ is the reduction reaction threshold, and $f(x_{NiO})$ is a function that depends on the morphology of nickel oxide particles.

During the primary reduction at temperatures of 400–600 °C, the reaction is described by the Avrami-Erofeev kinetics [27, 28], which means that the function $f(x_{NiO})$ has the following form:

$$f(x_{NiO}) = x_{NiO} (\ln x_{NiO})^{\frac{m-1}{m}}, \tag{3}$$

where $m \approx 0.6$. When re-reduced at high temperatures, the reaction can be considered to have first-order kinetics, i.e., $f(x_{NiO}) = x_{NiO}$.

Diffusion

The molar flux of hydrogen in the sample substrate was calculated from Fick's law:

$$J_{\mathrm{mol}} = -D_{\mathrm{eff}}/RT \nabla p_{H_2}, \tag{4}$$

where $D_{\mathrm{eff}} = D\frac{\varepsilon}{\tau^2}$ is the effective diffusion coefficient of hydrogen in the pores of the substrate, ε is the porosity of the sample, and τ is its tortuosity.

In the process of reduction, the porosity of the sample changes, since the molar volume of metallic nickel is 41% less than that of its oxide [29]. Knowing the ratio of NiO and YSZ in cermet, as well as the initial sample porosity ε_0, it is possible to calculate the porosity depending on the fraction of reduced NiO:

$$\varepsilon = \varepsilon_0 + 0.41\varepsilon_{\mathrm{NiO}}(1 - x_{\mathrm{NiO}}), \tag{5}$$

where $\varepsilon_{\mathrm{NiO}}$ is the volume fraction of nickel oxide in the sample.

The effective diffusion coefficient was calculated using a three-dimensional cube packing model [30], from which follows the expression for the tortuosity of the sample through its porosity

$$\tau = \frac{1 + \varepsilon^2}{\varepsilon(1 + \varepsilon)^2 + 4\varepsilon^2(1 - \varepsilon)}, \tag{6}$$

Gas transport

The very fast kinetics of the process leads to the fact that the rate of the reduction reaction is often determined by the rate of hydrogen supply and water removal, and the design of the working chamber plays an important role in this. The gas supply system can be characterized by the relative pressure drop $\frac{p_0 - p_s}{p_0}$, where p_0 is the partial pressure of hydrogen in the supplied mixture and p_s is the average partial pressure of hydrogen on the sample surface, depending on the fraction of consumed hydrogen ϑ_{H_2}. This dependence can be considered linear except for the region of high fuel consumption coefficients:

$$\vartheta_{H_2} = k_{tr}\frac{p_0 - p_s}{p_0}, \tag{7}$$

In order to optimize the experiment, a model of hydrogen distribution in the gas chamber was calculated depending on the distance from the gas tube to the sample. As a result of this estimation, it was found that the optimal distance is 0.5 cm. From one point of view, k_{tr} for such an optimal distance is close to 1, and from another point of view, hydrogen

and water concentration anode area distributions are uniform enough to apply the one-dimensional model. Also, within the framework of this model, it was found that the use of a mixture of hydrogen and nitrogen as a fuel mixture leads to a decrease in k_{tr} for all considered distances.

For a better interpretation of the measurement results, a calibration procedure was carried out to find k_{tr} of the given system. Namely, for the reduced state of the anode, the fuel flow was varied at direct current, and the voltage at direct current was measured.

Simplified reaction rate calculation

Assuming linear kinetics, the model equations at the initial moment of time give the following expression for the reduction rate:

$$Q = \frac{(1 + \gamma)^{-1}}{(kp_0 l_f S_a \tanh\frac{a}{l_f})^{-1} + (k_{tr}R_0)^{-1}}, \tag{8}$$

where $k = \frac{k_c S_V x_{\mathrm{NiO}}}{RT}(1 + \gamma)$, $l_f = \sqrt{\frac{D_{\mathrm{eff}}}{k_c S_V x_{\mathrm{NiO}}}}$ is the reaction front depth, S_a is the sample area, a is its thickness, and R_0 is the hydrogen flow entering the working chamber (mol/s).

Expression Eq. (8) is applicable only at the initial stage of the reaction, but gives us opportunity to note the characteristic dependencies that are also valid for the full model.
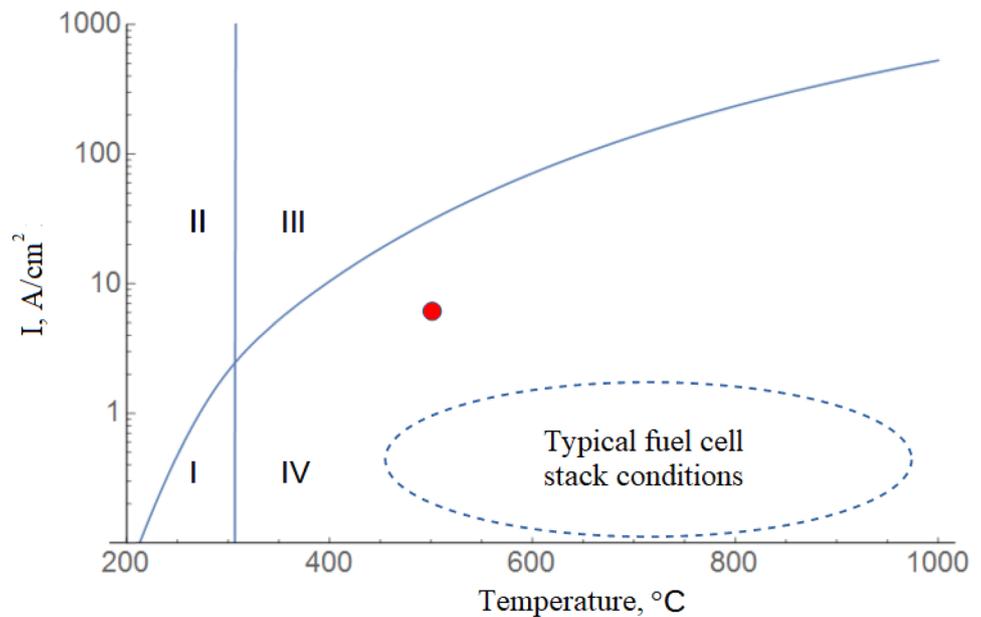
Experimental validation

According to the developed model, the reduction reaction can take place in one of 4 modes (Fig. 4) depending on the temperature and the amount of fuel supplied:

(I) Uniform reduction throughout the entire volume of the sample, the reaction rate is limited by the amount of hydrogen supplied.

(II) Uniform reduction over the entire volume of the sample, the reaction rate is limited by the kinetics of the NiO particle reduction reaction.

(III) The reduction proceeds as a front, the reaction rate is limited by the kinetics of the front movement.

(IV) The reduction proceeds as a front, the reaction rate is limited by the amount of supplied hydrogen.

From the point of view of reduction kinetics studies, the experiment in mode II is the most reliable, since in this mode diffusion through the pores and the supply of hydrogen are fast enough not to affect the reaction rate. In this way, we will obtain the most relevant data on the reaction rate, without additional uncertainty, since the reaction rate in this mode does not depend on the unknown effective diffusion

Fig. 4 The reduction mode depends on the temperature and hydrogen flow into the working chamber in terms of the equivalent electric current (A/cm^2). The dot marks the conditions of the redox experiments described below

coefficient. However, in order to expand the boundaries of region II to a temperature of 600 °C, it is necessary to consider thin samples (10–20 μm) with a higher porosity. On the other hand, at small x_{NiO}, the reaction rate drops sufficiently to get into region II.

Note that under typical SOFC conditions, the reaction proceeds in mode IV, from which it is difficult to extract the reaction kinetics. In order for the reaction to proceed in mode III, it is possible to increase the hydrogen flow and decrease the area of the sample, its porosity, and also, the partial pressure of hydrogen.

Within the framework of the model developed, a series of experiments were carried out, including the cycling of the sample at 500 °C in redox atmospheres with the measurement of the OCV. Each cycle consisted of complete reduction of the sample in 100% H$_2$ and subsequent partial oxidation in 100% O$_2$ for various time intervals from 0.25 to 14 h. The experimental conditions are marked in Fig. 4 with a dot in region IV.

Figure 5 shows the dependence of the OCV on time during the reduction process. Each curve corresponds to different initial fraction of oxidized nickel. Let us note that the curves behave similarly. The abrupt initial voltage growth corresponds to the growth of hydrogen concentration in the anode chamber. Then, small peak follows probably corresponding to NiO reduction initiation stage. After that, almost linear growth of OCV ends by inflection point (maximum of second derivative). Finally, OCV asymptotically tends to stable value. In the following, we assume that reduction process is divided to two stages. The first stage is front-like reduction in the regime IV. During this stage, the major part of NiO reduces. At the second

stage, the remaining NiO with low access to gas phase reduces. This assumption is in agreement with TG analysis of reduction process. In the following, we will provide the evidence that inflection point of OCV corresponds to switching from the first stage of reduction process to the second.
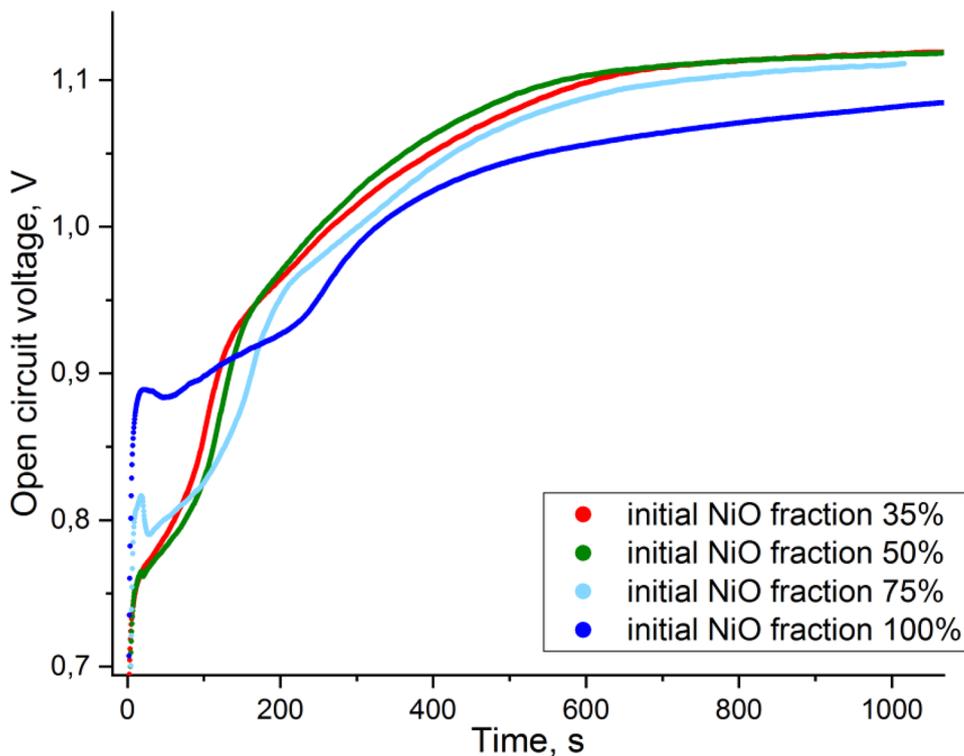
The initial oxidized Ni fraction in the samples is estimated from the time of oxidation using thermogravimetrical curves for Ni oxidation process from [29].

The oxidation of the sample in pure oxygen occurs almost uniformly, while in the case of oxidation in air, the reaction proceeds with a front from the surface. This difference is caused by the fact that pure oxygen is delivered to the sample volume by convective flows, whereas the presence of ballast gas leads to the oxygen partial pressure drop in the sample inner layers.

At first stage of the reduction process, the rate of reduction is almost constant and determined by the reaction threshold pressure of hydrogen $p_{H_2}^{th}$. To determine it, let us find the fraction of utilized hydrogen ϑ_{H_2} during first stage of the reduction process. One can find ϑ_{H_2} comparing the dependence of the measured time of the reduction process first stage with the estimated sample reduction time in the 100% utilization of hydrogen assumption. In that way from Fig. 6 follows $\vartheta_{H_2} = 0.49 \pm 0.05$. Then, one can use the measured value of $k_{tr} = 1.10 \pm 0.02$ and expression (7) to find $\gamma = \frac{p_{H_2}^{th}}{p_{H_2O}^{th}} = 1.24 \pm 0.08$. This value is in good agreement with the data from [26].

As for the graphs of the OCV curves (Fig. 7), one can notice a common characteristic feature for all cycles: this is a linear section ending in a sharp rise in the OCV. The linear

Fig. 5 Time dependence of OCV for 4 reduction processes with different initial fraction of oxidized Ni in the sample

sections on all reduction curves have the same height, and their slope is inversely proportional to the recovery time. This can be interpreted as the movement of the reduction front at a constant speed in the presence of a constant ion current of about 300 µA/cm^2 through the YSZ subgrid of the sample.

Fig. 6 Dependence of the time of the reduction process first stage on the estimated sample reduction time in the 100% utilization of hydrogen assumption. It is assumed that the reduction process first stage ends at the inflection point of OCV from Fig. 5
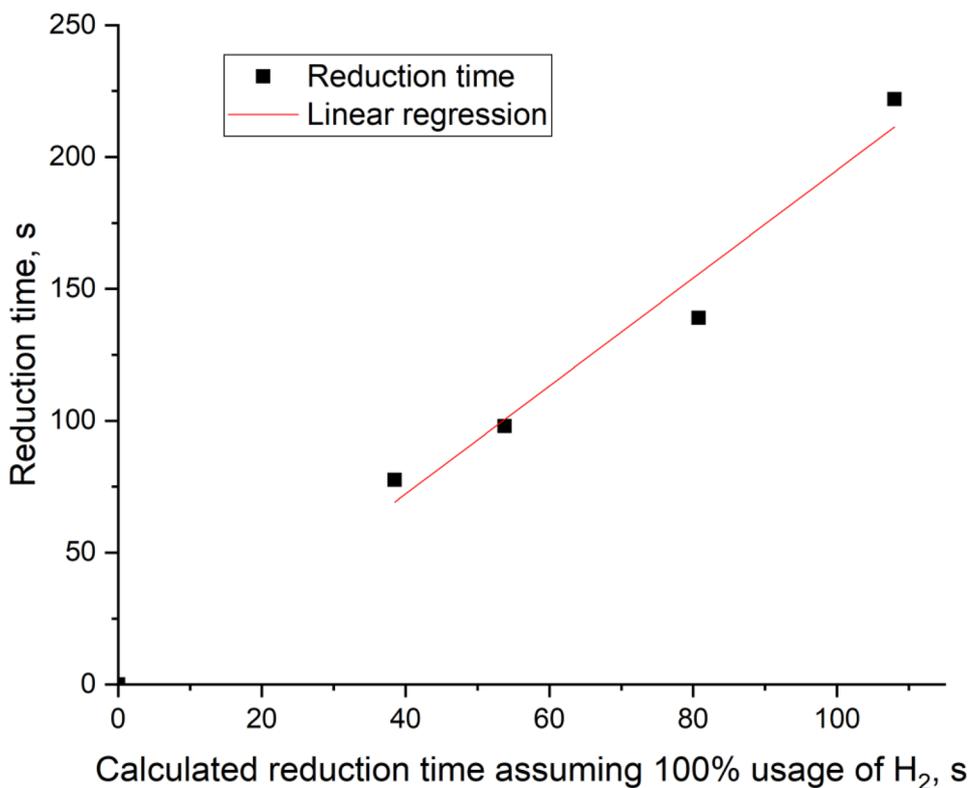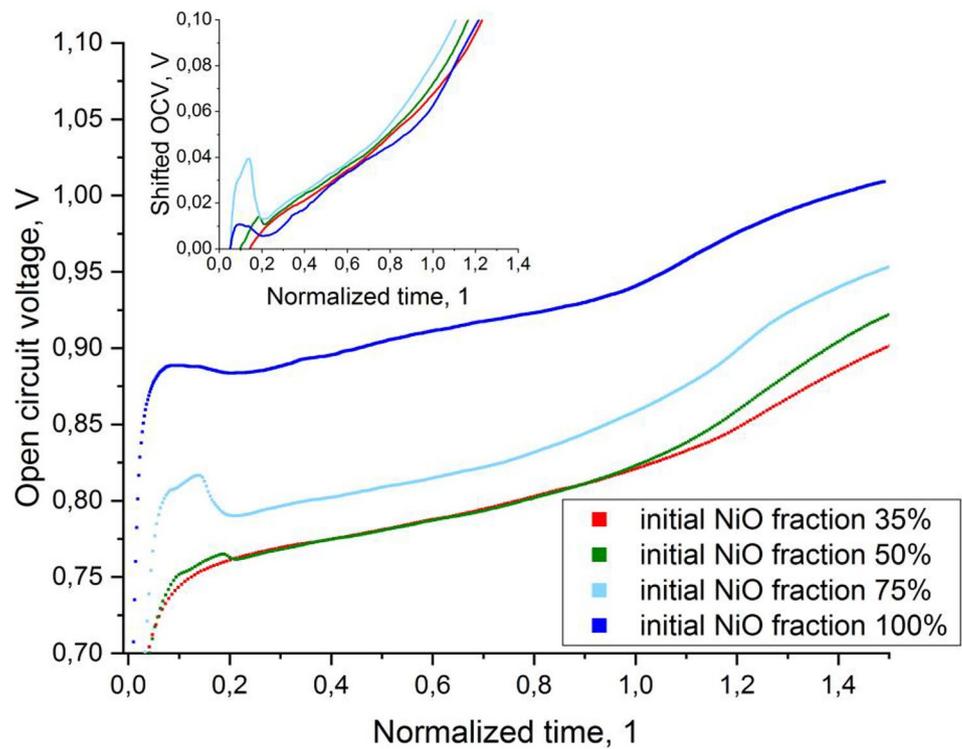
Fig. 7 Dependence of the OCV on the time normalized by the time of the sample reduction process first stage. Curves are shifted along the voltage axis to compare the slope

During the initial reduction of the sample, Raman spectra were obtained (Fig. 8). We followed the peak in the region of 1100 cm^{-1} Raman shift, which corresponds to the longitudinal two-phonon vibrations of nickel oxide [31].

Intensity of 1100 cm^{-1} line for metallic nickel is much lower than that for NiO. Then, by the time of the disappearance of

Fig. 8 Raman spectra collected during the primary reduction of the anode-supported SOFC. Working temperature is 600 °C; fuel gas is H$_2$ with the flow of 100 ml/min. Raman peaks around 180, 300, and 600 cm^{-1} correspond to lattice vibrations of zirconia in the electrolyte material, the studied NiO peak is noted in the region of 1100 cm^{-1}

this peak, one can follow the appearance of metallic nickel at the anode|electrolyte inner interface. According to our model, the peak disappearance time corresponds to the reduction of the surface layer of nickel oxide particles with a thickness of 25 ± 5 nm. On the other hand, the light penetration depth in Ni is given by the following expression:

$$\delta = \frac{\lambda}{2\pi \, \text{Im} \, \widetilde{n}} \tag{8}$$

where $\lambda = 532$nm is the laser wavelength and $\widetilde{n}$ is the complex refractive index. An estimate using expression Eq. (8) and data for refractive index from [32] give a value of about $\delta = 24$nm, which is in good agreement with the data obtained by Raman spectroscopy.
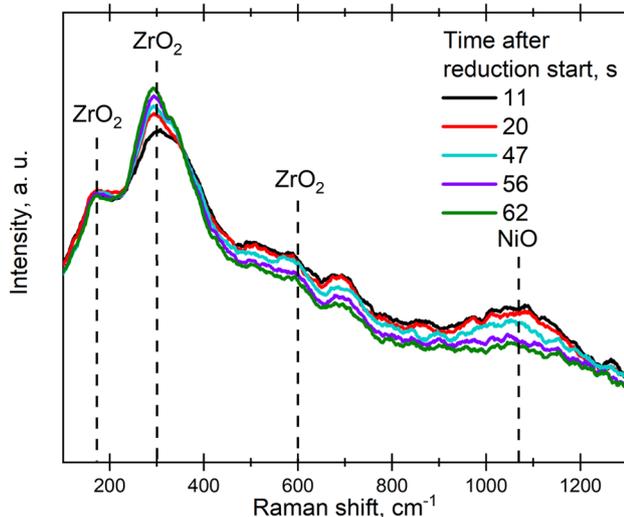
Conclusions

Within the framework of this work, a model for the reduction of the cermet composite Ni-YSZ SOFC anode substrate was developed. Based on this model, the reduction processes can take place in four modes, depending on the temperature and flow of the supplied fuel. At temperatures lower than 300 °C and fuel flows lower than 30 ml/min in the geometry of our experimental stand, reduction occurs uniformly over the entire sample, and the kinetics of the process is limited by the amount of supplied hydrogen. With an increase in hydrogen flows, the kinetics of the NiO particle reduction

reaction become significant. In the region of higher temperatures, a reduction front already takes place, the movement of which is limited either by the amount of fuel supplied or by its own kinetics of movement.

It has been found that the high rate of the NiO reduction reaction requires a higher hydrogen flux per unit area of the sample for direct kinetic measurements. From electrochemical measurements, according to the model, confirmation of the previous assumptions about the front movement was obtained. It has been shown to move at a constant speed.

The value of the reduction reaction threshold in the mode of hydrogen deficiency, obtained in the work, is consistent with the literature. Based on the data from the Raman spectra, calculations were made for the thickness of the reduced NiO layer, which are in good agreement with the thickness of the Ni skin layer.

References

1. The Bloom Energy Server 5 Datasheet (2022) https://www.bloomenergy.com/wp-content/uploads/es5-300kw-datasheet-2022.pdf
2. Götz T, Saurat M, Kaselofsky J, Obernberger I, Brunner T, Weiss G, Bellostas BC, Moretti C (2019) First stage environmental impact assessment of a new highly efficient and fuel flexible medium-scale CHP technology based on fixed-bed updraft biomass gasification and a SOFC. ETA-Florence Renewable Energies 1586–1594. https://doi.org/10.5071/27thEUBCE2019-4DO.2.4
3. Mastropasqua L, Campanari S, Valenti G, Guariniello A, Modena S, Ghigliazza F (2016) Testing and preliminary modelling of a 2.5 kW micro-CHP SOFC unit. ASME 2016 14th Int Conf Fuel Cell Sci Eng Technol. https://doi.org/10.1115/fuelcell2016-59327
4. Kaur G (2015) SOFC Technology: its working and components. Solid Oxide Fuel Cell Components. 79–122. https://doi.org/10.1007/978-3-319-25598-9_3
5. Burmistrov I, Agarkov D, Bredikhin S, Nepochatov Yu, Tiunova O, Zadorozhnaya O (2013) Multilayered electrolyte-supported SOFC based on NEVZ-ceramics membrane. ECS Trans 57(1):917–923. https://doi.org/10.1149/05701.0917ecst
6. Burmistrov IN, Agarkov DA, Tsybrov FM, Bredikhin S (2016) Preparation of membrane-electrode assemblies of solid oxide fuel cells by co-sintering of electrodes. Russ J Electrochem 52(7):669–677. https://doi.org/10.1134/s1023193516070053
7. Burmistrov IN, Agarkov DA, Korovkin EV, Yalovenko DV, Bredikhin S (2017) Fabrication of membrane-electrode assemblies for solid-oxide fuel cells by joint sintering of electrodes at high temperature. Russ J Electrochem 53(8):873–879. https://doi.org/10.1134/s1023193517080043
8. Yamaji K, Kishimoto H, Xiong Yu, Horita T, Sakai N, Yokokawa H (2004) Performance of anode-supported SOFCs fabricated with EPD techniques. Solid State Ionics 175(1–4):165–169. https://doi.org/10.1016/j.ssi.2004.09.032
9. Song JH, Park SI, Lee JH, Kim HS (2008) Fabrication characteristics of an anode-supported thin-film electrolyte fabricated by the tape casting method for IT-SOFC. J Mater Process Technol 198(1–3):414–418. https://doi.org/10.1016/j.jmatprotec.2007.07.030
10. Matsuda M, Hosomi T, Murata K, Fukui T, Miyake M (2007) Fabrication of bilayered YSZ/SDC electrolyte film by electrophoretic deposition for reduced-temperature operating anode-supported SOFC. J Power Sources 165(1):102–107. https://doi.org/10.1016/j.jpowsour.2006.11.087
11. Chen K, Chen X, Lü Z, Ai N, Huang X, Su W (2008) Performance of an anode-supported SOFC with anode functional layers. Electrochim Acta 53(27):7825–7830. https://doi.org/10.1016/j.electacta.2008.05.063
12. Gamova AA, Eliseeva GM, Burmistrov IN, Agarkov DA, Ionov UV, Solovyov AA, Tartakovskii II, Bredikhin SI (2019) Study of the kinetics of the formation of the electric potential of anode-supported SOFCs by Raman spectroscopy and electrochemical measurements. The 6th Russian conference with international participation "Fuel cells and power plants based on them." 193–195. ISBN 978–5–6040595–3–1. https://doi.org/10.26201/ISSP.2019/FC.35
13. Agarkov DA, Burmistrov IN, Tsybrov FM, Tartakovskii II, Kharton VV, Bredikhin SI (2017) In-situ Raman spectroscopy analysis of the interfaces between Ni-based SOFC anodes and stabilized zirconia electrolyte. Solid State Ionics 302:133–137. https://doi.org/10.1016/j.ssi.2016.12.034
14. Agarkov DA, Burmistrov IN, Tsybrov FM, Tartakovskii II, Kharton VV, Bredikhin SI (2016) Kinetics of NiO reduction and morphological changes in composite anodes of solid oxide fuel cells: estimate using Raman scattering technique. Russ J Electrochem 52(7):600–605. https://doi.org/10.1134/s1023193516070028
15. Agarkov DA, Burmistrov IN, Tsybrov FM, Tartakovskii II, Bredikhin SI (2016) SOFC membrane-electrode assembly. Russian Patent 161095
16. Bredikhin SI, Agarkov DA, Burmistrov IN, Eliseeva GM, Solovyov AA, Ionov UV (2019) SOFC membrane-electrode assembly with thin-film electrolyte for optical studies. Russian Patent 189528
17. Agarkov DA, Burmistrov IN, Tsybrov FM, Kveder VV, Bredikhin SI (2016) Device for investigation electrochemical and optical characteristics of SOFCs. Russian Patent 165785
18. Gamova AA, (2019) Study of the kinetics of formation of residues on SOFC anode-supporting structure of the Raman method and electrochemical measurements. Bachelor thesis.
19. Kceracell (2015) http://kceracell.com/pdf/2015_Kceracell.pdf. Accessed 18 Oct 2022
20. Kceracell (2015) http://kceracell.com/cathode.html. Accessed 18 Oct 2022
21. Eliseeva GM, Agarkov DA, Burmistrov IN, Gamova AA, Ionov IV, Rabotkin SV, Bredikhin SI (2019) Raman spectra studies of inner "anode | electrolyte" interface on ESC and ASC SOFCs. ECS Trans 91(1):457–469. https://doi.org/10.1149/09101.0457ecst
22. Agarkov DA, Burmistrov IN, Eliseeva GM, Ionov IV, Rabotkin SV, Semenov VA, Bredikhin SI. (2020) Comparison of in-situ Raman studies of SOFC with thick single-crystal and thin-film magnetron sputtered membranes. Solid State Ion 344:115091. https://doi.org/10.1016/j.ssi.2019.115091
23. Eliseeva GM, Burmistrov IN, Agarkov DA, Gamova AA, Ionov IV, Levin MN, Solovyev AA, Tartakovskii II, Kharton VV, Bredikhin SI (2020) In-situ Raman spectroscopy studies of oxygen spillover at solid oxide fuel cell anodes. Chemical Problems 1(18):9–19. https://doi.org/10.32737/2221-8688-2020-1-9-19
24. Korableva GM, Agarkov DA, Burmistrov IN, Lomonova EE, Maksimov AA, Samoilov AV, Solovyev A, Tartakovskii II, Kharton VV, Bredikhin SI (2021) Application of high-temperature Raman spectroscopy (RS) for studies of electrochemical processes in solid oxide fuel cells (SOFCs) and functional properties of their components. ECS Trans 103(1):1301–1317. https://doi.org/10.1149/10301.1301ecst
25. Rashed AH, Rao YK (1997) Kinetics of reduction of nickel oxide with hydrogen gas in the 230–452°C range. Chem Eng Commun 156(1):1–30. https://doi.org/10.1080/00986449708936666
26. Hidayat T, Rhamdhani MA, Jak E, Hayes PC (2009) The kinetics of reduction of dense synthetic nickel oxide in H2–N2 and H2–H2O atmospheres. Metall Mater Trans B 40(1):1–16. https://doi.org/10.1007/s11663-008-9212-0

27. De Bruijn TJW, De Jong WA, Van Den Berg PJ (1981) Kinetic parameters in Avrami—Erofeev type reactions from isothermal and non-isothermal experiments. Thermochim Acta 45(3):315–325. https://doi.org/10.1016/0040-6031(81)85091-5

28. Ortega A, Maqueda LP, Criado JM (1995) The problem of discerning Avrami-Erofeev kinetic models from the new controlled rate thermal analysis with constant acceleration of the transformation. Thermochim Acta 254:147–152. https://doi.org/10.1016/0040-6031(94)02068-y

29. Waldbilling D, Wood A, Ivey D (2005) Thermal analysis of the cyclic reduction and oxidation behaviour of SOFC anodes. Solid State Ionics 176(9–10):847–859. https://doi.org/10.1016/j.ssi.2004.12.002

30. Kong W, Zhang Q, Xu X, Chen D (2015) A simple expression for the tortuosity of gas transport paths in solid oxide fuel cells' porous electrodes. Energies 8(12):13953–13959. https://doi.org/10.3390/en81212406

31. Mironova-Ulmane N, Kuzmin A, Steins I, Grabis J, Sildos I, Pärs M (2007) Raman scattering in nanosized nickel oxide NiO. J Phys Conf Ser 93:012039. https://doi.org/10.1088/1742-6596/93/1/012039

32. Johnson B, Christy RW (1974) Optical constants of transition metals: Ti, V, Cr, Mn, Fe Co, Ni, and Pd. Phys Rev B 9:5056